Computational simulation of fluid and dilute particulate flows on spiral concentrators

B.W. Matthews [a,b], C.A.J. Fletcher [a,*], A.C. Partridge [b]

[a] Centre for Advanced Numerical Computation in Engineering and Science, University of New South Wales, Sydney, NSW 2052, Australia

[b] School of Mining Engineering, University of New South Wales, Sydney 2052, Australia

Abstract

Spiral separators are used globally in the fine coal and heavy mineral processing industries as gravity-concentration devices. Consisting of an open trough that spirals vertically downwards in helix configuration about a central axis, a slurry mix of particles and water is fed to the top of the concentrator. Particles are then separated radially on the basis of density and size as they gravitate downwards. To enhance performance, the geometric design has evolved historically by experimental trial-and-error investigations to develop a prototype suited to the given industrial application. This approach has proved somewhat prohibitive for design purposes however, and researchers have accordingly turned to numerical techniques in an attempt to develop a fully predictive and reliable model for use in the design process. Towards this end, the present paper uses Computational Fluid Dynamics (CFD) analysis to simulate fluid and dilute particulate flows on one operational spiral unit. The free-surface Volume-of-Fluid (VOF) algorithm, isotropic RNG $k–\varepsilon$ turbulence model and Lagrangian method have been used for this purpose. Satisfactory predictions have been obtained with respect to a collaborative experimental program, and the model forms the basis for future examination of the two-way fluid-particle coupling processes and inter-particle effects. © 1998 Elsevier Science Inc. All rights reserved.

Keywords: Spiral concentrator; Computational fluid dynamics; Free-surface flow; Volume-of-fluid (VOF) method; RNG $k–\varepsilon$ turbulence model; Lagrangian particulate analysis

1. Introduction

The generic geometry of spiral concentrators consists of an open trough that spirals vertically downwards in helix configuration about a central axis. Employed in the fine coal and heavy mineral processing industries, a slurry mix of fine particles (75–3000 μm) is fed to the top of the spiral and, as it gravitates downwards, particles are segregated radially across the trough by the centrifugal force. Separation occurs as light suspended particles travel to the outer trough regions whilst heavy particles settle and tend to move inwards towards the central column. Historically, evolution of the design has been almost exclusively based on empirical development of the appropriate geometry. However, because this approach has proven to be expensive, time-con-

* Corresponding author. Tel.: +61 2 9318 0004; fax: +61 2 9319 2328; e-mail: bwm.cances.atp.com.au.

suming and hence somewhat prohibitive, optimal designs have not been necessarily achieved. The past decade has therefore seen developments in theoretical flow investigations, of which Computational Fluid Dynamics (CFD) has particular benefit because the detailed flow and particulate interactions in complex domains can be solved using only the fundamental governing equations.

Following the analytical study of Holland-Batt [1], researchers of concentrator flows have employed numerical techniques in response to the continuing rapid advance of computer hardware in recent years. Although providing valuable insights into the mechanisms of spiral concentrator operation, the analytical approaches are limited for predictive purposes because they require significant empirical input. Following Wang and Andrews [2], who used CFD to determine the flow fields for simplified rectangular spiral sections, Jancar et al. [3] examined the fluid flow on the coal-concentrating LD9 spiral using their locally developed code. As part of an ongoing research program, the present paper further examines the flow on the LD9 unit using, instead, the commercial CFD program, FLUENT, and the more robust Volume-of-Fluid (VOF) method for modelling the free surface transport. This paper extends the preliminary qualitative fluid flow study of Matthews et al. [4] in which laminar solutions were presented. Quantitative fluid flow predictions have now been enabled using the RNG k–ε turbulence model and particulate flow analyses have also been conducted at dilute concentration.

2. Governing equations

2.1. Fluid flow

Spiral concentrator flows possess a free-surface, have shallow depths of <1 cm typically, and display laminar to increasingly turbulent behaviour radially outwards with velocities reaching 3 m/s [1,5]. A secondary circulation current in a plane perpendicular to the mainstream flow direction, induced by the spiral curvature and resultant centrifugal force, travels outwards near the free-surface and back inwards towards the central column near the trough base. To model this flow, the fluid phase is considered Newtonian, to possess constant physical properties and to be governed by the Reynolds-averaged turbulent Navier–Stokes equations. The steady-state equations for the conservation of mass and momentum in generalised curvilinear form, are respectively given by:

$$\frac{\partial \rho u_i}{\partial x_i} = 0, \tag{1}$$

$$\frac{\partial}{\partial x_j}(\rho u_i u_j) = -\frac{\partial P}{\partial x_i} + \rho g_i + \frac{\partial}{\partial x_j}\left[\mu_{\text{eff}}\left(\frac{\partial u_i}{\partial x_j} + \frac{\partial u_j}{\partial x_i}\right)\right], \tag{2}$$

where ρ is the fluid density, μ_{eff} the effective (molecular μ plus turbulent μ_t) viscosity, P the static pressure, and u_{ij}, and g_i the mean velocity and gravitational acceleration, respectively. To consider the effects of turbulence, the isotropic eddy viscosity concept and dynamic renormalisation group theory (RNG) based k–ε turbulence model [6] have been employed. This model contains very few empirically adjustable parameters and is therefore applicable to a wide range of flow situations. The local level of turbulence kinetic energy (k) and energy dissipation rate (ε) are solved using the following transport equations:

$$\rho \frac{\partial}{\partial x_j}(u_j k) = \frac{\partial}{\partial x_j}\left(\alpha_k \mu_{\text{eff}} \frac{\partial k}{\partial x_j}\right) + \mu_t P_k - \rho\varepsilon, \tag{3}$$

$$\rho \frac{\partial}{\partial x_j}(u_j \varepsilon) = \frac{\partial}{\partial x_j}\left(\alpha_\varepsilon \mu_{\text{eff}} \frac{\partial \varepsilon}{\partial x_j}\right) + C_1 \frac{\varepsilon}{k}\mu_t P_k - C_2 \rho \frac{\varepsilon^2}{k} - R, \tag{4}$$

with

$$P_k = \left(\frac{\partial u_j}{\partial x_i} + \frac{\partial u_i}{\partial x_j}\right)\frac{\partial u_j}{\partial x_i}, \quad R = \frac{c_\mu \rho \eta^3 (1 - \eta/\eta_0)\varepsilon^2}{1 + C_3 \eta^3 k}, \quad \eta = \sqrt{P_k}\frac{k}{\varepsilon}, \tag{5}$$

where P_k is the turbulence production and R an additional rate of strain term. According to the RNG theory, the constants in the turbulent transport equations are given as $C_1 = 1.42$, $C_2 = 1.68$, $C_3 = 0.012$, $\eta_0 = 4.38$, and $C_\mu = 0.085$. The turbulence is more sensitive to the mean rate-of-strain than the standard k–ε model because of R in the ε transport equation (4). The RNG formulation, by theoretical derivation, naturally accounts for the laminar, transitional and turbulent flow regions. Moreover, α_k and α_ε are variables determined locally throughout the flow, enabling the effects of streamline curvature to be considered in the analysis. The equation for μ_{eff} expressed in approximate algebraic form is given by:

$$\mu_{\text{eff}} = \mu \left[1 + \sqrt{\frac{c_\mu}{\mu}\frac{k}{\sqrt{\varepsilon}}}\right]^2. \tag{6}$$

2.2. Particulate flow

In this paper, the Lagrangian method has been used to simulate the particulate flow at dilute concentration on the LD9 spiral. The trajectory of an individual dispersed particle is calculated by integration of the force balance on the particle to equate its inertia and, in curvilinear non-orthogonal form, this balance may be expressed by [7]:

$$\frac{\mathrm{d}u_{\mathrm{p}}^i}{\mathrm{d}t} = \left(\frac{p_{\mathrm{f}}}{\rho_{\mathrm{p}}}\right)u_{\mathrm{p}}^i \frac{\partial u_{\mathrm{f}}^i}{\partial x_i} + \frac{1}{2}\frac{\rho_{\mathrm{f}}}{\rho_{\mathrm{p}}}\frac{\mathrm{d}}{\mathrm{d}t}\left(u_{\mathrm{f}}^i - u_{\mathrm{p}}^i\right) + \frac{3\mu_{\mathrm{f}}C_{\mathrm{D}}\mathrm{Re}_{\mathrm{p}}}{4\rho_{\mathrm{p}}D_{\mathrm{p}}^2}\left(u_{\mathrm{f}}^i - u_{\mathrm{p}}^i\right) + \left(\frac{\rho_{\mathrm{p}} - \rho_{\mathrm{f}}}{\rho_{\mathrm{p}}}\right)g_i. \tag{7}$$

Strictly, this equation describes the forces acting on a particle ($_{\mathrm{p}}$) by the undisturbed flow and is applicable to a rigid sphere smaller than the characteristic eddy size of the turbulent motion [7]. The term on the left-hand-side is the particle inertia, defining the force required to accelerate the sphere of diameter D_{p} through the fluid. The forces on the right-hand-side of Eq. (7) represent respectively, the pressure gradient in the fluid, virtual mass required to accelerate the fluid surrounding the particle, Stokes steady-state viscous drag, and buoyancy due to gravity. Re_{p} is the particle Reynolds number and C_{D} the drag coefficient given by:

$$\mathrm{Re}_{\mathrm{p}} = \frac{\rho_{\mathrm{f}}D_{\mathrm{p}}\left|\left(u_{\mathrm{p}}^i - u_{\mathrm{f}}^i\right)\right|}{\mu_{\mathrm{f}}}, \tag{8}$$

$$C_{\mathrm{D}} = \frac{a_1 + a_2}{\mathrm{Re}_{\mathrm{p}}} + \frac{a_3}{\mathrm{Re}_{\mathrm{p}}^2} \tag{9}$$

in which a_1, a_2 and a_3 are coefficients dependent upon Re_{p} and given by Morsi and Alexander [8]. To predict the turbulent dispersion of particles, the mean fluid velocity and instantaneous value of the fluctuating component has been employed using a stochastic Continuous Random Walk model [9]. In this model, the reduced time available for interaction between a particle and an eddy, by the "crossing trajectory" effect of gravity has also been considered. Because particles have been investigated at dilute concentrations they are assumed to have negligible influence upon the fluid flow field.

3. Boundary conditions

To solve Eqs. (1)–(9), appropriate boundary conditions must be employed in the flow domain. At the spiral inlet all fluid velocity components have been specified and the distribution of F defined to give a desired flow rate (see following sub-section). At the exit, mainstream gradients of the velocity components have been set to zero and no-slip conditions imposed at solid surfaces. For next-to-wall cells placed at y^+-values $\geqslant 11.6$, the wall function approach has been used to link the flow with the near wall profiles of velocity and turbulence parameters. For cells placed at $y^+ < 11.6$, the laminar stress condition has been employed instead. Special consideration of the boundary conditions at the free surface and during a particle-wall collision is provided below.

3.1. Free-surface treatment

A wide range of methods have been developed to model the transient motion of free surfaces. Each technique possesses strengths and weaknesses that limit them to specific types of flow, although Eulerian methods have been the most widely used and comprise fixed-grid and adaptive-grid formulations [10]. For modelling spiral concentrator flows, Jancar et al. [3] have successfully employed an Eulerian adaptive-grid technique in which the computational grid is adjusted locally as part of the solution process to follow the free-surface. The interface is a well-defined continuous curve upon which boundary conditions can be accurately implemented and small distortions detected between nodes on the mesh. However, difficulties can arise in adjusting the grid to follow interfaces that are highly deformed and, for this reason, the Jancar model has encountered numerical instabilities when resolving concentrator flows of high curvature [4].

For the purposes of design, a more robust method for simulating the free-surface transport has therefore been sought by the authors. Indeed, a fixed-grid Eulerian method, the Volume-of-Fluid (VOF) formulation devised by Hirt and Nichols [11] has been preferred. In this method, the interface between two phases (water and air) is tracked on a mesh that remains fixed so that the interface does not usually coincide with a grid line. Numerical stability is generally easily obtained because the flow field calculations are not coupled with identification of the free surface location. The VOF method has been successfully employed in other applications, including axisymmetric flows [12], the splashing of droplets [13], the sloshing of fluid in containers [14], and flows in pressure vessels and piping systems [11].

The philosophy behind the VOF method is to define a function F throughout the computational domain whose value is unity at any point occupied by the fluid of interest, and zero otherwise. The average value of F in a cell represents the fractional volume of that cell occupied by the fluid, with values between zero and one containing the free surface. Evolution of the F field is governed by the following transport equation:

$$\frac{\partial F}{\partial t} + u_i \frac{\partial F}{\partial x_i} = 0. \tag{10}$$

A single momentum equation (2) is solved throughout the domain, and the resulting velocity field is shared by the two phases. The momentum equation is dependent upon the volume fraction F through the properties ρ and μ. These properties are defined in each cell using the following relations, in which the subscripts w and a refer to the water and air phases, respectively:

$$\rho_{\text{cell}} = F\rho_{\text{w}} + (1 - F)\rho_{\text{a}},$$

$$\mu_{\text{cell}} = F\mu_{\text{w}} + (1 - F)\mu_{\text{a}}. \tag{11}$$

Computationally, the VOF method is economical because the free-surface location is neither directly calculated nor stored during the solution process. Instead, the interface is reconstructed whenever necessary by using a straight line through each relevant cell, the location and slope of which are determined by both the cell value and local gradients of *F*. This process is less accurate than the direct methods of calculation employed by adaptive grid techniques. After the free surface location has been determined, the velocities and pressure in cells that contain the interface are then assigned to ensure satisfaction of the complete free surface stress conditions [15]. Assuming that viscous stresses in air are several orders of magnitude smaller than stresses in the liquid, and that the curvature of the free surface is small, the normal and tangential stress conditions can be expressed as:

$$P = P_0 + 2\mu \frac{\partial u_n}{\partial n},$$ (12)

$$\frac{\partial u_{t1}}{\partial n} + \frac{\partial u_n}{\partial t_1} = 0,$$

$$\frac{\partial u_{t2}}{\partial n} + \frac{\partial u_n}{\partial t_2} = 0,$$ (13)

in which *P* denotes the required free surface pressure, P_0 the ambient air pressure, u_n the normal free surface velocity component, and u_{t1} and u_{t2} the tangential free surface velocity components. At steady-state, the interface is at ambient pressure and behaves as a symmetry plane with normal gradients of all variables equal to zero. Although viscous stresses and surface tension cannot be simulated accurately because the interface within each cell is not located precisely, these forces have been justifiably neglected as Froude numbers across the trough are >1.0. Moreover, although details of the interface smaller than the grid size cannot be resolved using the VOF technique, this limitation has been largely overcome by using very fine meshes.

3.2. Particulate–wall interaction

As discussed by Brauer [16], a large number of factors influence the dynamics of a particle–wall collision. Some of the important parameters include the collision angle, particle translational and rotational velocities, properties of the particle and wall materials, particle shape, and wall roughness. Too little experimental information exists to allow detailed realistic modelling of a collision and so assumptions generally need to be made of the dynamics involved [17]. The approach used here is that outlined by Matsumoto and Saito [18] and subsequently employed by Tsuji et al. [19], Oesterle [20] and Sommerfield [17]. Specifically, impulse equations describing the interaction between smooth walls and spherical particles are used to determine the particulate translational velocities after impact. Two types of collision are distinguished by the presence or not of sliding at the point of contact. A collision without sliding takes place when the following condition is satisfied:

$$\left| u_{T,1} - \left(\frac{D_p}{2} \omega_1 \right) \right| < \frac{7}{2} \phi_0 (1 + e) u_{N,1},$$ (14)

in which $u_{T,1}$ is the particulate tangential velocity to the wall immediately prior to the collision, D_p the particle diameter, ω the angular velocity, ϕ_0 the static coefficient of wall friction, *e* the particulate restitution coefficient describing the elasticity or otherwise of the collision, and $u_{N,1}$ the initial normal velocity to the wall of the particle. Eq. (14) reveals that at acute impact angles (α), sliding will usually predominate but the rotation of the particle and friction at the wall must also be considered. Following Sommerfield [17], it is useful to represent Eq. (14) graphically by
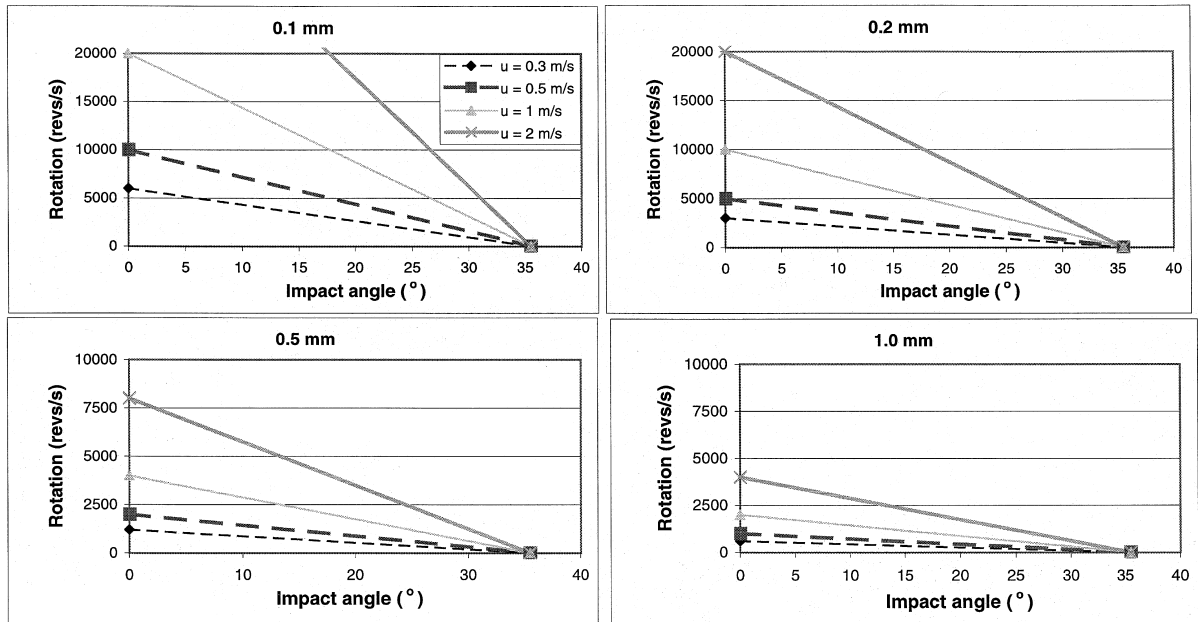
Fig. 1. Influence of particle rotation on the type of collision for particle diameters of 0.1–1.0 mm and tangential impact velocities of 0.3–2.0 m/s. Values above and below each curve reflect non-sliding and sliding upon impact, respectively.

relating α, ω, ϕ_0 and D_p to the type of collision. This is demonstrated in Fig. 1 for $u_{T,1}$ velocities characteristic for the LD9 unit of 0.3, 0.5, 1.0, and 2.0 m/s, and particle sizes of 100, 200, 500 and 1000 µm. Having assumed values for e and ϕ_0 of 1.0 and 0.2, respectively, values below each curve indicate sliding upon impact whilst values above are indicative of non-sliding.

It can be observed in Fig. 1 that for smaller particle sizes and greater approach velocities, higher values of ω are required to prevent sliding. Additionally, the critical angular velocity reduces as the impact angle increases. Rotational velocities of particles have not been measured on spiral concentrators so it is necessary to provide an estimate in the present analysis. If it is assumed that zero slip occurs, then ω can be approximated by the velocity divided by D_p [21]. Characteristic values of ω within the inner, mid and outer trough regions for particle sizes of 100, 200, 500 and 1000 µm are given in Table 1. Except for the largest particles occurring within the inner radial regions, impact angles have been found to be sufficiently acute ($\alpha < 10°$) so that sliding collisions predominate (c.f. Fig. 1). Moreover, the estimates of ω given in Table 1 are probaly maximum values as significant slip could be expected on the hydraulically smooth fi-

Table 1
Estimated rotational velocities (revs/s) for 100–1000 µm particles within the inner (0.05 m radius), mid (0.15 m) and outer (0.25) trough regions on the LD9 unit

Radial position	Particle diameter (µm)			
	100	200	500	1000
Inner	3400 (0.34)	1800 (0.36)	780 (0.39)	410 (0.41)
Mid	6000 (0.60)	4000 (0.80)	1800 (0.90)	1000 (1.00)
Outer	9000 (0.9)	6000 (1.20)	2800 (1.40)	1600 (1.60)

Bracketed values represent mainstream fluid velocities (m/s) used to calculate ω.

breglass walls of the concentrator, particularly at the high impact velocities and acute incidence angles typically encountered. Moreover, realistic non-spherical particles will rotate less than spheres and have a preferred orientation within the flow.

Accordingly, rotational velocities are assumed to play a minor role in the collision dynamics, and the translational velocity components immediately after sliding (indicated by subscript 2) are then given as [18]:

$$u_{N,2} = -eu_{N,2}, \tag{15}$$

$$u_{T,2} = u_{T,1} - [\phi_d(1 + e)u_{N,1}Z_0], \tag{16}$$

$$Z_0 = \text{sign}\left[u_{T,1} - \left(\frac{D_p}{2}\omega_1\right)\right], \tag{17}$$

in which Eq. (17) serves as a lower limit for $u_{T,2}$ where the velocity cannot be reduced below that due to the assumed rotational velocity (Table 1); it also accounts for particles that have settled to the trough base and are rolling downstream. In the above equations, the only empirical values are the coefficients of restitution (e) and dynamic friction (ϕ_d). Although e is dependent upon the impact velocity and material properties of the particle and wall, at low values of α ($<15°$) the restitution coefficient is not particularly sensitive to variations of these parameters [16]. Moreover, although the normal coefficient (e_n) is related to the deformation of the wall material whilst the tangential component (e_t) is related separately to the friction coefficient, at $\alpha < 20°$ $e_n = e_t = e$ [16]. The dependence of e upon the impact angle is assumed to follow the relation obtained by Grant and Tabakoff [22] for quartz sand impacting on Aluminium alloy:

$$e = 0.993 - 1.76\alpha + 1.56\alpha^2 - 0.49\alpha^3, \tag{18}$$

where α is expressed in radians. Although this relationship reveals that for $\alpha = 90°$, e is 0.18, at high impact angles the restitution coefficient is known to vary substantially depending upon the particular combination of materials considered [16]. However, the value of 0.18 is similar to the equivalent measurements for coal and waste rock samples [23] and also the value of 0.2 used by Beck and Holtham [24] in their computational simulations of coal stratification in a batch jig. The employed value for ϕ_d of 0.1 is the same as that used by [24] and is consistent with values obtained for spheres impacting upon smooth plates [25].

4. Definition of domain and numerical procedure

The LD9 computational domain uses a single block, structured, curvilinear 3D grid (Fig. 2). For computing purposes, the spiral has been divided into 35° sections with the computed outlet solution specified as the inlet conditions for the next downstream sector. The domain is bounded by four walls and the flow is essentially a duct flow that includes an interface between water and air. The model irrelevantly calculates the air flow solution but because grid cells are stretched in the depth-wise direction toward the spiral base, the computing time to do this is minimised. Because of its greater inertia, and because no surface shear is specified at the free surface, the liquid flow is not influenced by the air flow.

The equations have been solved using a finite volume method on a non-staggered grid. The primitive flow field and VOF distributions were solved implicitly in which convective first derivatives were calculated using a second to third order QUICK discretisation scheme; three point symmetrical formulae were used to discretise the second derivatives. The velocity fields were determined from Eq. (2) using the iterative Line–Gauss–Seidel scheme and a velocity potential
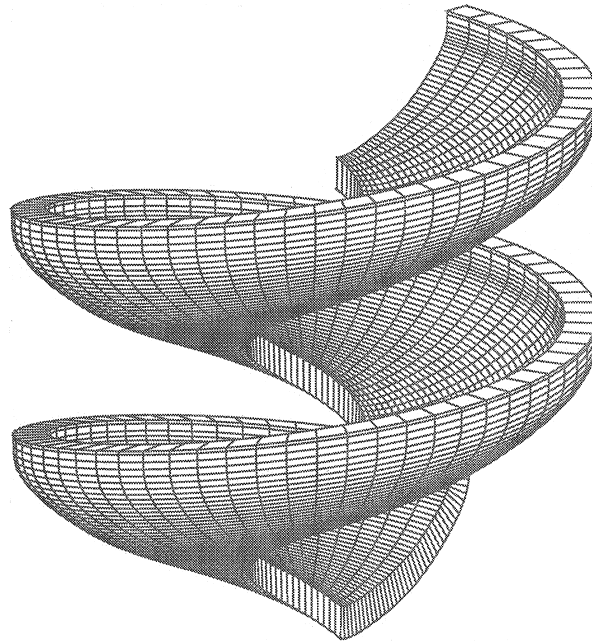
Fig. 2. Computational domain for two turns of the LD9 concentrator unit, with reduced cells for clarity.

correction introduced to satisfy continuity (1) and to upgrade the pressure field using the SIMPLE algorithm.

After the volume fraction F had been calculated and the free surface position located, boundary conditions at the interface were used to determine the pressure and velocities within the surface cells (Eqs. (12) and (13)). The primitive flow variables were then updated and the process repeated until neither the flow field nor the free surface profile changed. For this purpose, all residuals were reduced to below 3×10^{-4} before transfer of the outlet results to the inlet plane of the next downstream sector. Typically, CPU times of 4 h were required to reach the fully-developed state and a further 2 h needed to transfer the results downstream on one 120 MHz processor of a Hewlett–Packard K210 Unix server.

Use of only the QUICK scheme in the solution process would have led to progressive smearing of the F function and loss of definition of the interface by dissipative and dispersive terms occurring in the truncation error. Accordingly, the Donor–Acceptor method [11] was used to compute F explicitly using a time-marching scheme after convergence in each sector. Typically, 50 time-steps of 0.001 s were needed for the interface to be convected from the inlet to outlet plane. In the Donor–Acceptor method, sharper resolution is attained by limiting the amount of fluid that can be convected across a cell face to the minimum of two values: the filled volume of the phase in the donor cell; or the free volume available in the acceptor cell.

The trajectories of individual particles were calculated in the fully-developed fluid flow domains for six complete spiral turns. Step-wise integrations over discrete time-steps were conducted using the fourth-order Runge–Kutta method. Integration of Eq. (7) yielded the velocity of the particle at each point along the trajectory and a further integration in time predicted the trajectory itself. The fluid velocity at the precise particulate position, estimated by a Taylor series expansion about the value stored at the cell-centre, was employed. Instantaneous values of the fluid velocity were also used and the trajectories of 100 particles with the same density and size calculated to account for the random effects of turbulence.

5. Results

Analyses have been performed by examining the fully-developed free-surface flow on the LD9 unit at industrial flow rates of 4, 6 and 8 m³/h. Substantial empirical data is available for validation of the model [5,26]. In the present study, the 35° section of the flow domain (Fig. 2) consists of a mesh with 20 × 39–46 × 208 control volumes in the mainstream, depth-wise and radial directions, respectively. The number of cells in the depth-wise direction has been varied according to the flow rate and these cells have been clustered toward the spiral base so that in the region of maximum water depth, 22–37 of the 39–46 cells contain water. The thin nature of the flow implied that the occurrence of high aspect ratios with respect to the cross-stream direction could not be avoided. Ratios of up to 15 existed in the domain but because depth-wise gradients of the flow variables were generally much greater than those in the other directions, the widely accepted limits of 5–10 were tolerably exceeded.

The cross-stream fluid flow profile at 6 m³/h and fully-developed state is depicted in Fig. 3. Induced by the centrifugal force, the water accumulates to the outer 20% of the concentrator and smoothly increases its depth (0–7.8 mm) outwards across the trough. Predicted and measured depths against radial distance (4 and 8 m³/h) are plotted in Fig. 4. Overall, satisfactory agreement is observed between the experimental and numerical results. The extent of water movement along the outer trough wall is predicted satisfactorily, and the inner radial depths (1–2 mm) are found to vary negligibly between flow rates. The greatest variation in depth between flow rates occurs in the outer regions, although the maximum predicted values of 5.5, 7.8 and 10.3 mm are less than those measured of 6.5, 9.0, and 14.0 mm [5].

The method of depth measurement employed by Holtham [5] consisted of conductivity probes immersed in the fluid. The probes were progressively lifted at small increments until conductivity ceased and the depths were considered accurate to the nearest 0.5 mm. Although this error cannot explain the significant discrepancy within the outer regions (Fig. 4), Holtham did observe the presence there of finely dispersed entrained air. Presumably, the presence of air pockets occurs as turbulent eddies are able to protrude above the free surface, entrapping air as they return as droplets to the medium [27]. In turbulent channel flow, the entrapped air increases the depth which at Froude numbers of 7–9 for the outer regions on the LD9 unit, translates empirically to
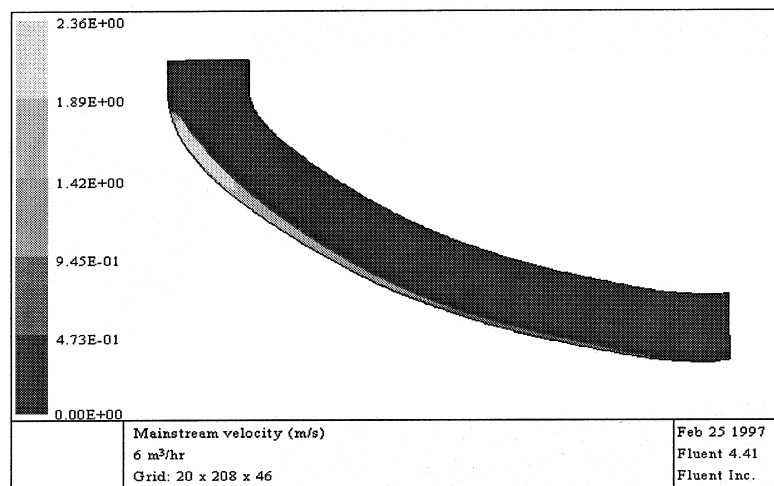

Fig. 3. Predicted transverse fluid profile and mainstream velocity distribution at 6 m³/h.
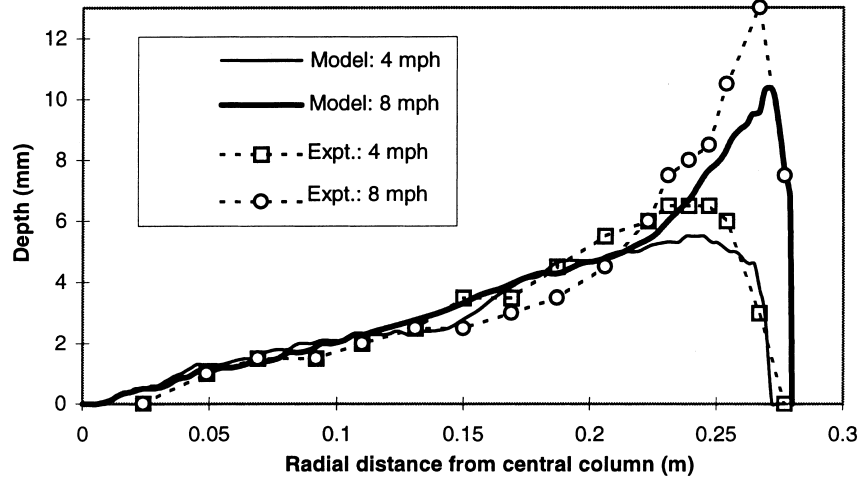
Fig. 4. Fluid depth profiles: experiment (Holtham, 1990) versus CFD model at flow rates of 4 and 8 m³/h.

an excess depth of approximately 15–20% [28]. Significantly, the apparent numerical and experimental discrepancy can then be explained by air entrainment which is currently unaccounted for by the model.

As the depth increases radially outwards, the trough wall has progressively less influence on the flow and the velocity increases. Accordingly, the flow moves from the laminar, transitional and fully turbulent regimes outwards across the trough. Holtham [5] attempted to calculate the boundaries of these flow regimes by using the relationship for Reynolds number, Re, in open channel flow, given by: $Re = \rho h V_M / \mu$ in which h is the local mean flow depth (Fig. 3) and V_M the mean velocity. Values of V_M for eight radial streams were determined by dividing the spiral into sections using vertical splitter plates, measuring the flow rates in each stream and estimating their cross-sectional area. Assuming that the transition from laminar to turbulent flow occurs in the range $400 < Re < 2000$, the transition supported by the injection of dye traces, was found to occur at 0.08–0.16 m radius with estimated error bounds of ±30%. Similarly, the computational equivalent of Re at 4 m³/h predicts the transition to occur at 0.04–0.14 m from the central column (Fig. 5).

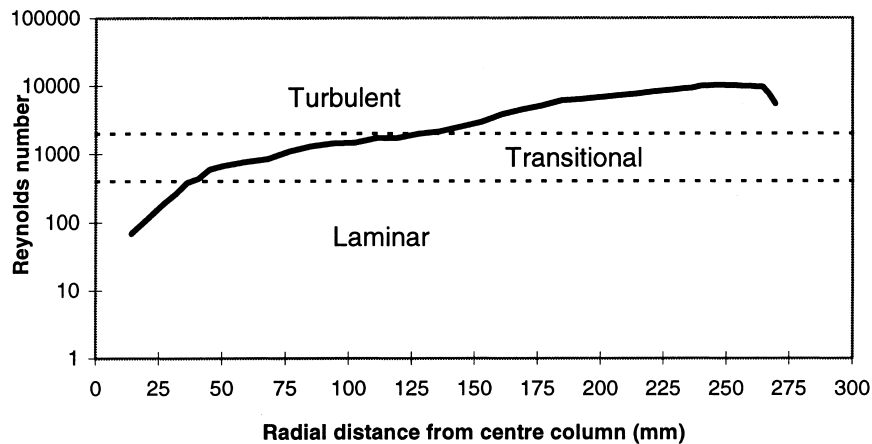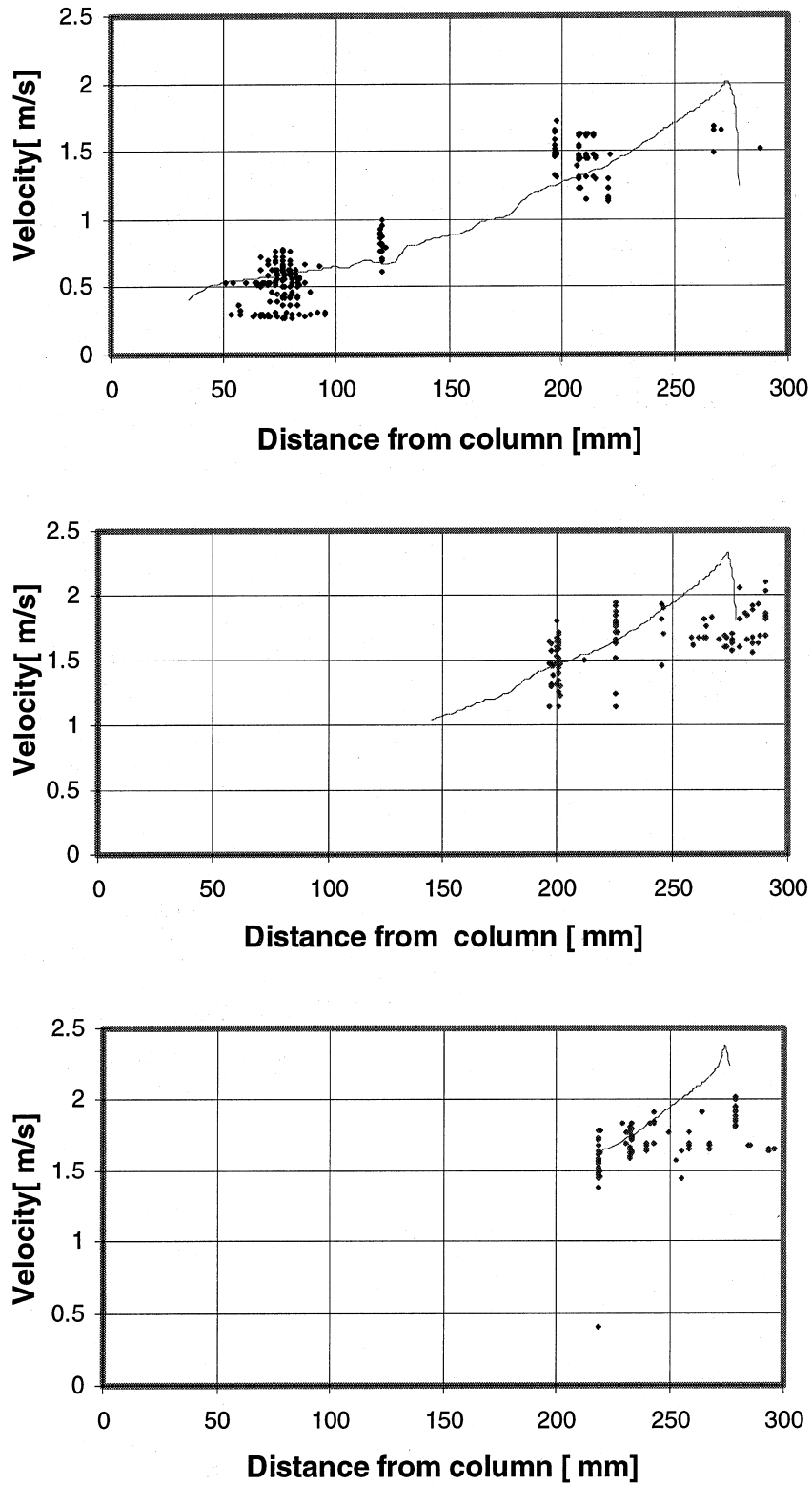Fig. 5. Predicted Reynolds number versus radial distance at 4 m³/h.

Fig. 6. Predicted and measured mainstream velocities at 6 m³/h: 1 mm depth (top); 3 mm depth (mid); 5 mm depth (bottom). Curves are mean numerical predictions. Measured points are instantaneous values.

The instantaneous values of the mainstream velocity (v) on the LD9 unit have been measured experimentally by Golab et al. [26] using Particle Image Velocimetry (PIV). The measurements are estimated to have reasonably small error ($<\pm20\%$), allowing the value of any given predictive model to be rigorously assessed. Similar to the empirical analysis, the model predicts the mainstream velocity to smoothly increase in magnitude outwards across the trough; the velocity distribution at 6 m³/h is depicted in Fig. 3. In general, the maximum velocity at any given radius occurs at the free surface and for the three flow rates investigated, increases from approximately 0.4 m/s in the innermost trough region, to its highest value near the outermost point of movement along the outer wall. Encouragingly, the maximum predicted values of 2.0, 2.4 and 2.6 m/s at respectively, 4, 6 and 8 m³/h are similar to the equivalent PIV measurements of 2.0, 2.3 and 2.2 m/s.

The validity of the model can perhaps be most rigorously tested by comparing the predicted distributions of v with the equivalent experimental measurements at arbitrary radii and depths within the flow. Simulations of the mean mainstream velocity and the comparative measured instantaneous values at 6 m³/h for depths of 1, 3 and 5 mm are plotted in Fig. 6. Qualitatively, the model seems to have predicted satisfactorily the mean profiles of velocity, the curves of which generally bisect the experimental values. Significant variation of the empirical data observed in Fig. 6 probably reflects a number of causes, including the genuine turbulent nature of the flow and error associated with the PIV technique in being able to resolve depths to only 0.5 mm [26].

The secondary circulation flow (u) on spiral concentrators occurs normal to the mainstream flow direction. Induced by the curvature of the channel, the centrifugal force (proportional to v^2 and hence maximum at the free surface and zero at the wall) tends to convey water radially outwards. Opposing forces due to gravity and pressure gradient are reasonably uniform over the full depth at any given radius so that the flow returns inwards near the trough base. Where these forces are equal and opposite at some fractional depth within the flow, u is zero. The model is able to capture the secondary motion, the structure of which in the outer region of the spiral is depicted in Fig. 7 at 8 m³/h. This classic structure extends to the innermost regions where depths are less than 1.5 mm, and the flow reversal occurs at fractional depths of 0.3–0.55.

Like its primary counterpart v, the strength of u increases with greater radius, is an order of magnitude smaller than v, and has been found to vary downstream even after the onset of de-
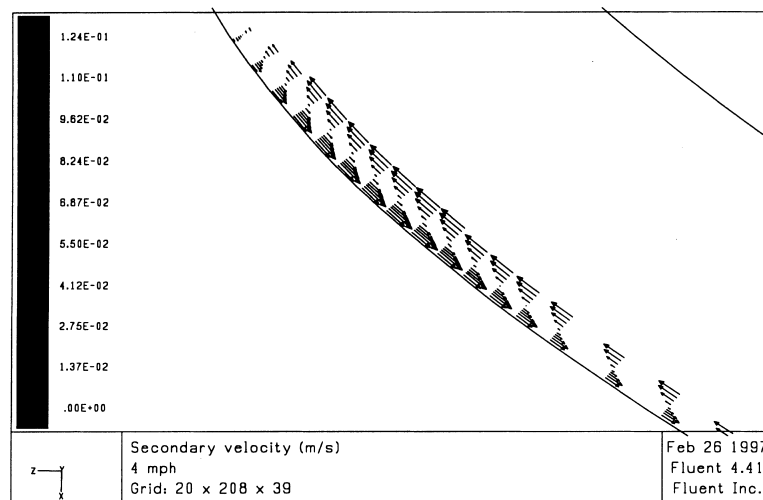

Fig. 7. Secondary flow in the outer trough at 4 m³/h. For clarity, the number of vectors has been reduced by respectively, factors of two and four in the depth-wise and cross-stream directions.

veloped flow conditions. At flow rates of 4, 6 and 8 m³/h respectively, mean values of u have been found to vary from 0.05–0.13, 0.05–0.22, and 0.05–0.25 m/s; the maximum outward velocity exists at the free surface and the comparative inward maximum at an approximate fractional depth of 0.1 (Fig. 7). These findings are consistent with measurements using the injection of dye traces [5] which demonstrate in particular that u is indeed an order of magnitude less than v. Although less capable of capturing the mean secondary flow behaviour, the PIV technique has also found u to be distinctly unsteady with variations of at least the same order as the mean values [26].

To examine the hydrodynamic influences on relative particulate separation, 100 particles have been input into the flow domain at 4 and 8 m³/h. Radial distributions across the trough were determined after the particles had travelled six complete turns down the spiral. Representing their positions of hydrodynamic equilibrium, analyses were performed for both coal particles ($\rho_p = 1450$ kg/m³) and quartz ($\rho_p = 2650$ kg/m³). These particles reflect the extremes of density processed on the LD9 unit, for which particle diameters of 100, 200, 500 and 1000 μm were examined. The resultant radial distributions are given in Fig. 8 for fluid flow rates of 4 and 8 m³/h; as yet experimental results from the collaborative research program are not available for comparison.

The predicted distributions in Fig. 8 clearly demonstrate the classic pattern observed on spiral separators, with finer and less dense particles migrating to the outer trough zones. Similarly to the numerical investigation of Holland-Batt [1], outward migration diminished rapidly above 500 μm for both particulate densities and flow rates. Above this limit, the particles were found to settle to the trough base and slide inwards toward the inner radii. Under all flow conditions the finest (100 μm) particles remained in suspension and migrated to the outer zones. Variations of flow rate and density were found to influence particles in the somewhat narrow size range of $200 < D_p < 500$ μm.

Initially, particles were injected at five radial locations from the innermost to outermost regions across the trough. Generally, particles migrated to their positions of hydrodynamic equilibrium
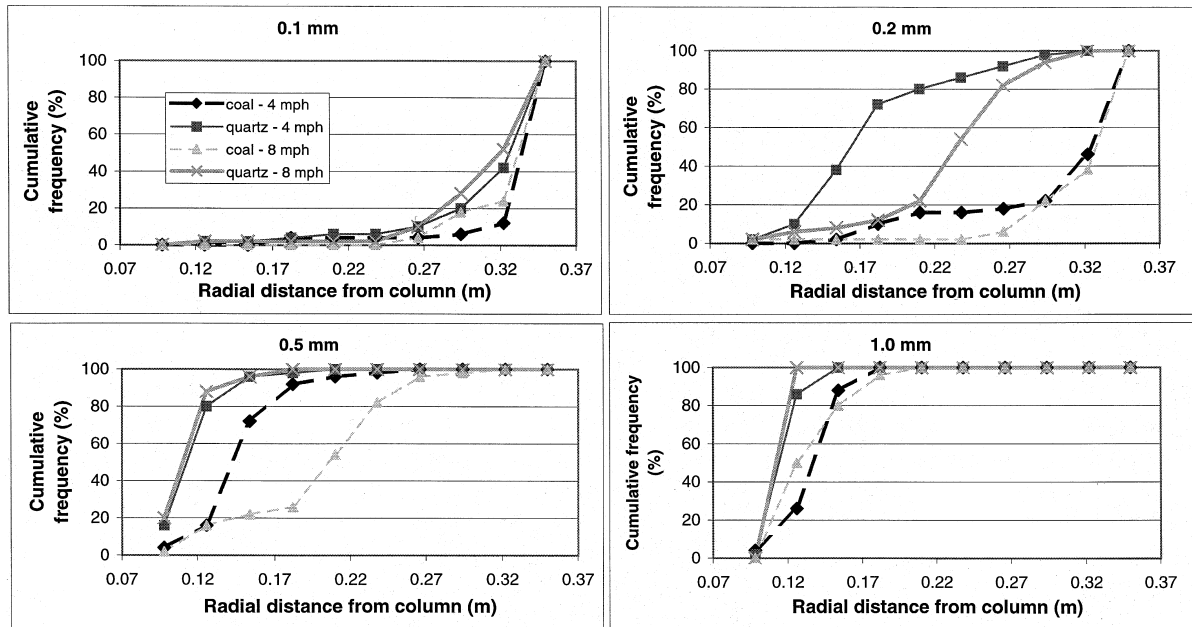

Fig. 8. Radial distributions of 0.1–1.0 mm diameter coal and quartz particles at fluid flow rates of 4 and 8 m³/h (mph).

within three to four turns of the spiral unit. Particles that did not remain in suspension were found to saltate or bounce along the trough base, although the larger particles settled within the inner regions and tended to roll downstream. In practice, particles at dilute concentration which do not settle to form a bed, will tend to keep bouncing for longer distances than that predicted by the model. Caused by deviations from particle sphericity and wall roughness, the reduced decay of bouncing has been accounted for in other studies by employing irregular bouncing models [17,19].

Although the model has not yet investigated the particle dynamics at high concentration, the results suggest that the LD9 unit could be improved as a separator of coal from waste rock. By hydrodynamic processes, the concentrator should ideally segregate particles in the range of 100–1500 μm with coal migrating to the outer radii, and quartz remaining within the inner regions [1,5]. Moreover, although increasing the flow rate appears to extend the upper extent of particulate separation from 200 to 500 μm (Fig. 8), no single definitive radial cut exists between the desired product and waste material. For example at 8 m³/h, maximum separation for 200 μm particles would be achieved at 0.27 m from the central column. Conversely, poor separation at 0.27 m would occur for particles of 500 μm diameter, for which segregation should be performed at 0.12 m radius according to the analysis.

6. Conclusions

A commercial CFD code, FLUENT, has been used to model the fluid and dilute particulate flow on the LD9 spiral used for fine coal processing. For a range of flow rates, the free surface flow has been simulated using a robust fixed-grid VOF method and RNG k–ε turbulence model. Sound quantitative agreement with experimental data has been obtained with respect to flow depths and, most encouragingly, instantaneous mainstream velocities at arbitrary radii and depths within the flow. The secondary current has been able to be captured, the magnitudes of which are of the same order as available experimental data. Particulate analyses using the Lagrangian method have displayed the correct qualitative flow behaviour but have yet to be compared quantitatively with the collaborative experimental program. Future developments of the model will focus upon the particulate phase at progressively higher and hence more realistic feed concentrations.

References

[1] A.B. Holland-Batt, Spiral separation: theory and simulation, Trans. Instn. Min. Metall. (Sect. C) 98 (1989) C46–60.
[2] J.W. Wang, J.R.G. Andrews, Numerical simulation of liquid flow on spiral concentrators, Min. Eng. 7 (1994) 1363–1386.
[3] T. Jancar, C.A.J. Fletcher, P.N. Holtham, J.A. Reizes, Computational and experimental investigation of spiral separator hydrodynamics, Proceedings of the XIX International Mineral Proc. Congress, San Francisco, 1995.
[4] B.W. Matthews, C.A.J. Fletcher, A.C. Partridge, T. Jancar, Computational simulation of spiral concentrator flows in the mineral processing industry, Proc. CHEMECA '96, Aust. Inst. Chem. Eng., Sydney, 1996.
[5] P.N. Holtham, The fluid flow pattern and particle motion on spiral separators, unpublished Ph.D. Thesis, University of New South Wales, 1990.
[6] V. Yakhot, S.A. Orszag, Renormalisation group analysis of turbulence, I. Basic theory, J. Sci. Comput. 1 (1) (1986) 1–51.
[7] M.R. Maxey, J.R. Riley, Equation of motion for a small rigid sphere in a non-uniform flow, Phys. Fluids 26 (4) (1983) 883–889.
[8] S.A. Morsi, A.J. Alexander, An investigation of particle trajectories in two-phase flow systems, J. Fluid Mech. 55 (2) (1972) 193–208.

[9] D.J. Thomson, Criteria for the selection of stochastic models of particle trajectories in turbulent flows, J. Fluid. Mech. 180 (1987) 529–556.

[10] J.M. Floryan, H. Rasmussen, Numerical Methods for viscous flows with moving boundaries, Appl. Mech. Rev. 42 (12) (1989) 323–341.

[11] C.W. Hirt, B.D. Nichols, Volume of Fluid (VOF) method for the dynamics of free boundaries, J. Comp. Phy. 39 (1981) 201–225.

[12] F. Mashayek, N. Ashgriz, A hybrid finite-element-volume-of-fluid method for simulating free surface flows and interfaces, Int. J. Num. Meth. Fluids 20 (1995) 1363–1380.

[13] N. Nishikawa, T. Suzuki, A. Suzuki, Numerical simulation of splash of droplet, Lecture Notes in Physics 264 (1986) 499–504.

[14] I.S. Parton, Application of the VOF method to the sloshing of a fluid in a partially filled cylindrical container, Int. J. Num. Meth. Fluids 7 (1987) 535–550.

[15] B.D. Nichols, C.W. Hirt, Improved free surface boundary conditions for numerical incompressible-flow calculations, J. Comp. Phy. 8 (1971) 434–448.

[16] H. Brauer, Report on investigations on particle movement in straight horizontal tubes, particle/wall collision and erosion of tubes and tube bends, J. Powder & Bulk Solids Tech. 4 (2/3) (1980) 3–12.

[17] M. Sommerfield, Modelling of particle-wall collisions in confined gas-particle flows, Int. J. Multiphase Flow 18 (6) (1992) 905–926.

[18] S. Matsumoto, S. Saito, Monte Carlo simulation of horizontal pneumatic conveying based on the rough wall model, J. Chem. Eng. Japan 3 (2) (1970) 223–230.

[19] Y. Tsuji, T. Oshima, Y. Morikawa, Numerical simulation of pneumatic conveying in a horizontal pipe, KONA 3 (1985) 38–51.

[20] B. Oesterle, Internal kinetic transfers in the dispersed phase of a low concentration suspension flow, Int. J. Multiphase Flow 15 (1989) 155–171.

[21] C.A. Shook, Experiments with concentrated slurries of particles with densities near that of the carrier fluid, Can. J. Chem. Eng. 63 (1985) 861–869.

[22] G. Grant, W. Tabakoff, Erosion prediction in turbomachinery resulting from environmental solid particles, J. Aircraft 12 (5) (1975) 471–478.

[23] Z. Volsicky et al., Properties of brown coals and accompanying waste rock and their utilisation in connection with separation by dry processes, 10th Int. Coal Prep. Congress, 1986, pp. 168–180.

[24] A.J.G. Beck, P.N. Holtham, Computer simulation of particle stratification in a two-dimensional batch jig, Min. Eng. 6 (5) (1993) 523–536.

[25] F. Yamamoto, A study of motion of a sphere in air flow through horizontal pipe, Bull. JSME 20 (253) (1986) 2055–2061.

[26] K.J. Golab, P.N. Holtham, J. Wu, Validation of a computer model of fluid flow on the spiral separator, Innovation in physical separation technologies, Richard Mozely Memorial Symp., Inst. Min. Metall. London, 1997.

[27] T. Gangadharaiah, N.S.L. Rao, K. Seetharamiah, Inception and entrainment in self-aerated flows, J. Hyd. Div. Proc. ASCE 96 (1970) 1549–1565.

[28] N.S.L. Rao, H. Kobus, Characteristics of self-aerated surface flows, Water and Waste Water, Current Research and Practice 10 (1973).